

Automated Digital Hair Removal by Threshold Decomposition and Morphological Analysis

Joost Koehoorn¹, André C. Sobiecki^{1()}, Daniel Boda², Adriana Diaconeasa², Susan Doshi⁴, Stephen Paisey⁵, Andrei Jalba³, and Alexandru Telea^{1,2}

¹ JBI Institute, University of Groningen, Groningen, The Netherlands
{j.koehoorn,a.c.telea,a.sobiecki}@rug.nl

² University of Medicine and Pharmacy ‘Carol Davila’, Bucharest, Romania
[{daniel.boda, adriana.diaconeasa}@umf.ro](mailto:{daniel.boda,adriana.diaconeasa}@umf.ro)

³ Eindhoven University of Technology, Eindhoven, The Netherlands
a.c.jalba@tue.nl

⁴ School of Computer Science and Informatics, Cardiff University, Cardiff, UK
doshisk@cardiff.ac.uk

⁵ School of Medicine, Cardiff University, Cardiff, UK
paiseysj@cf.ac.uk

Abstract. We propose a method for digital hair removal from dermoscopic images, based on a threshold-set model. For every threshold, we adapt a recent gap-detection algorithm to find hairs, and merge results in a single mask image. We find hairs in this mask by combining morphological filters and medial descriptors. We derive robust parameter values for our method from over 300 skin images. We detail a GPU implementation of our method and show how it compares favorably with five existing hair removal methods.

Keywords: Hair removal · Threshold sets · Morphology · Skeletonization

1 Introduction

Automatic analysis of pigmented skin lesions [13, 7] occluded by hair is a challenging task. Several *digital hair removal* (DHR) methods address this by finding and replacing hairs by plausible colors based on surrounding skin. However, DHR methods are challenged by thin entangled, or low-contrast hairs [18, 27, 14, 11, 2, 12].

We address the above problems by converting the skin image into a threshold-set and adapting a gap-detection technique to find hairs in each threshold layer. Found gaps are merged into a single hair mask, where we find actual hairs by using 2D medial axes, and finally remove them by image inpainting.

Section 2 reviews related work on digital hair removal. Section 3 details our method. Section 4 presents its implementation. Section 5 compares our results with five DHR methods and also shows an extra application for CBCT image restoration. Section 6 discusses our method. Section 7 concludes the paper.

2 Related Work

In the past decade, many DHR methods have been proposed. DullRazor finds dark hairs on light skin by morphological closing using three structuring elements

that model three line orientations [18]. Different morphological operators were used in [22,19]. Hairs are removed by bilinear [18] or PDE-based inpainting [26]. Prewitt edge detection [14] and top-hat filtering [27] help finding low-contrast or thin-and-curled hairs. Huang *et al.* find hairs by multiscale matched filtering and hysteresis thresholding and remove these by PDE-based inpainting [12]. However, this method is quite slow (minutes for a typical dermoscopy image). VirtualShave finds hairs by top-hat filtering, like [27], and uses three density, sphericity, and convex-hull sphericity metrics to separate true positives (hairs) from other high-contrast details (false positives) [11]. Abbas *et al.* find hairs by a derivatives-of-Gaussian (DOG) filter [1,2]. However, this method has many parameters whose setting is complex. Finding other elongated objects such as arterial vessels and fibers is also addressed by path opening methods [8] and grayscale skeletons [10]. The last method also permits filling thin gaps similar to our hairs.

Table 1 captures several aspects of the above DHR methods. As visible, there is little comparison across methods. As method implementations are not publicly available (except [18,12]), comparison is hard. Hence, for our new DHR method outlined next, one main aim is to show how it compares to all reviewed methods.

Table 1. Comparison of existing digital hair removal methods

Method	Hair detector	Inpainting by	Compared with	# test images	Implementation
DullRazor [18]	generalized morphological closing	bilinear interpolation	—	5	available
Huang <i>et al.</i> [12]	multiscale matched filters	median filtering	DullRazor	20	available
Fioresi <i>et al.</i> [11]	top-hat operator	PDE-based [4]	DullRazor	20	not available
Xie <i>et al.</i> [27]	top-hat operator	anisotropic diffusion [20]	DullRazor	40	not available
E-shaver [14]	Prewitt edge detector	color averaging	DullRazor	5	not available
Abbas <i>et al.</i> [2]	derivative of Gaussian	coherence transport [5]	DullRazor, Xie <i>et al.</i> [27]	100	not available
Our method	gap-detection by multiscale skeletons	fast marching method [24]	DullRazor, Xie <i>et al.</i> [27], Huang <i>et al.</i> [12], Fioresi <i>et al.</i> [11], Abbas <i>et al.</i> [2]	over 300	available

3 Proposed Method

Most DHR methods find hairs by local luminance analysis (see Tab. 1, column 2). Such methods often cannot to find hairs that have *variable* color, contrast, thickness, or crispness across an image. Hence, our main idea is to perform a conservative hair detection at all possible luminance values. For this, we propose the following pipeline. First, we convert the input image into a luminance threshold-set representation (Sec. 3.1). For each threshold layer, we find thin hair-like structures using a morphological gap-detection algorithm (Sec. 3.2). Potential hairs found in all layers are merged in a mask image, which we next analyze to remove false-positives (Sec. 3.3). Finally, we remove true-positive hairs by using a classical image inpainting algorithm (Sec. 3.4). These steps are discussed next.

3.1 Threshold-Set Decomposition

We reduce color images first to their luminance component in HSV space. Next, we compute a threshold-set model of the image [28]: Given a luminance image $I : \mathbb{R}^2 \rightarrow \mathbb{R}_+$ and a value $v \in \mathbb{R}_+$, the threshold-set $T(v)$ for v is defined as

$$T(v) = \{\mathbf{x} \in \mathbb{R}^2 | I(\mathbf{x}) \geq v\}. \quad (1)$$

For n -bits-per-pixel images, Eqn. 1 yields 2^n layers $T_i = T(i), 0 \leq i < 2^n$. We use $n = 8$ (256 luminances). Note that $T_j \subset T_i, \forall j > i$, i.e. brighter layers are ‘nested’ in darker ones. If $I(\mathbf{x}) \neq i, \forall \mathbf{x} \in \mathbb{R}^2$, we find that $T_i = T_{i+1}$. In such cases, we simply skip T_i from our threshold-set decomposition, as it does not add any information. Our decomposition $\{T_i\}$ will thus have at most 2^n layers.

3.2 Potential Hair Detection

We find thin-and-long shapes in each layer T_i by adapting a recent gap-detection method [23], as follows.

Original Gap-Detection. Given a binary shape $\Omega \subset \mathbb{R}^2$ with boundary $\partial\Omega$, we compute the *open-close* image $\Omega_{oc} = (\Omega \circ H) \bullet H$ and *close-open* image $\Omega_{co} = (\Omega \bullet H) \circ H$. Here, \circ and \bullet denote morphological opening and respectively closing with a disk of radius H as structuring element. In both Ω_{oc} and Ω_{co} , small gaps get filled; yet, Ω_{co} has more gaps filled than Ω_{oc} , but also fills shallow concavities (dents) along $\partial\Omega$. Next, the skeleton or medial axis $S_{\Omega_{oc}}$ of Ω_{oc} is computed. For this, we first define the distance transform $DT_{\partial\Omega} : \mathbb{R}^2 \rightarrow \mathbb{R}_+$ as

$$DT_{\partial\Omega}(\mathbf{x} \in \Omega) = \min_{\mathbf{y} \in \partial\Omega} \|\mathbf{x} - \mathbf{y}\|. \quad (2)$$

The skeleton S_Ω of Ω is next defined as

$$S_\Omega = \{\mathbf{x} \in \Omega | \exists \mathbf{f}_1, \mathbf{f}_2 \in \partial\Omega, \mathbf{f}_1 \neq \mathbf{f}_2, \|\mathbf{x} - \mathbf{f}_1\| = \|\mathbf{x} - \mathbf{f}_2\| = DT_{\partial\Omega}(\mathbf{x})\} \quad (3)$$

where \mathbf{f}_1 and \mathbf{f}_2 are the contact points with $\partial\Omega$ of the maximally inscribed disc in Ω centered at \mathbf{x} . From $S_{\Omega_{oc}}$, the algorithm removes branch fragments that overlap with Ω , yielding a set $F = S_{\Omega_{oc}} \setminus \Omega$ that contains skeleton-fragments located in thin *gaps* that cut *deeply* inside Ω . To find all pixels in the gaps, the proposed method convolve the pixels $\mathbf{x} \in F$ with disk kernels centered at the respective pixels and of radius equal to $DT_{co}(\mathbf{x})$. As shown in [23], this produces an accurate identification of deep indentations, or gaps, in Ω , while ignoring pixels in shallow dents along $\partial\Omega$.

Hair-Detection Modification. We observe that, in a binary image with hairs in foreground, hairs are gaps of surrounding background. We next aim to find robustly hairs in all layers T_i . For this, several changes to [23] are needed. First, we note that [23] uses $DT_{\Omega_{co}}$ as disk-radius values for gap-filling as they argue that Ω_{co} closes more gaps than Ω_{oc} , supported by the observation that $DT_{\Omega_{co}}(\mathbf{x}) \geq DT_{\Omega_{oc}}(\mathbf{x}), \forall \mathbf{x} \in F$. Yet, for our hair-removal context, using $DT_{\partial\Omega_{co}}$ on every layer T_i , and next merging gaps into a single hair-mask, results in too

many areas being marked as hair. The resulting mask proves to be too dense – thus, creates too many false-positive hairs for our next filtering step (Sec. 3.3). Using the smaller $DT_{\partial\Omega_{oc}}$ as disk radius prevents this problem, but fails to find many hair fragments – thus, creates too many false-negatives. To overcome these issues, we propose to use a linear combination of $DT_{\partial\Omega_{oc}}$ and $DT_{\partial\Omega_{co}}$. In detail, we define a set of pairs disk-centers \mathbf{x} and corresponding disk-radii ρ as

$$D_\lambda = \{(\mathbf{x}, \rho = (1 - \lambda)DT_{\partial\Omega_{co}}(\mathbf{x}) + \lambda DT_{\partial\Omega_{oc}}(\mathbf{x})) \mid \mathbf{x} \in F\} \quad (4)$$

where $\lambda \in [0, 1]$ gives the effect of $DT_{\partial\Omega_{oc}}$ and $DT_{\partial\Omega_{co}}$ to the disk radius. A value of $\lambda = 0.2$, found empirically (see Sec. 6), avoids finding too many gaps (false-positives), while also preventing too many false-negatives.

Let D be the union of pixels in all disks described by D_λ . We next find the gaps G that potentially describe hairs as the difference

$$G = D \setminus \Omega. \quad (5)$$

We apply Eqn. 5 to compute a gap G_i from every shape $\Omega_i := T_i$. Next, we merge all resulting gaps G_i together into a single hair-mask image $M = \bigcup_{i=0}^{2^n} G_i$.

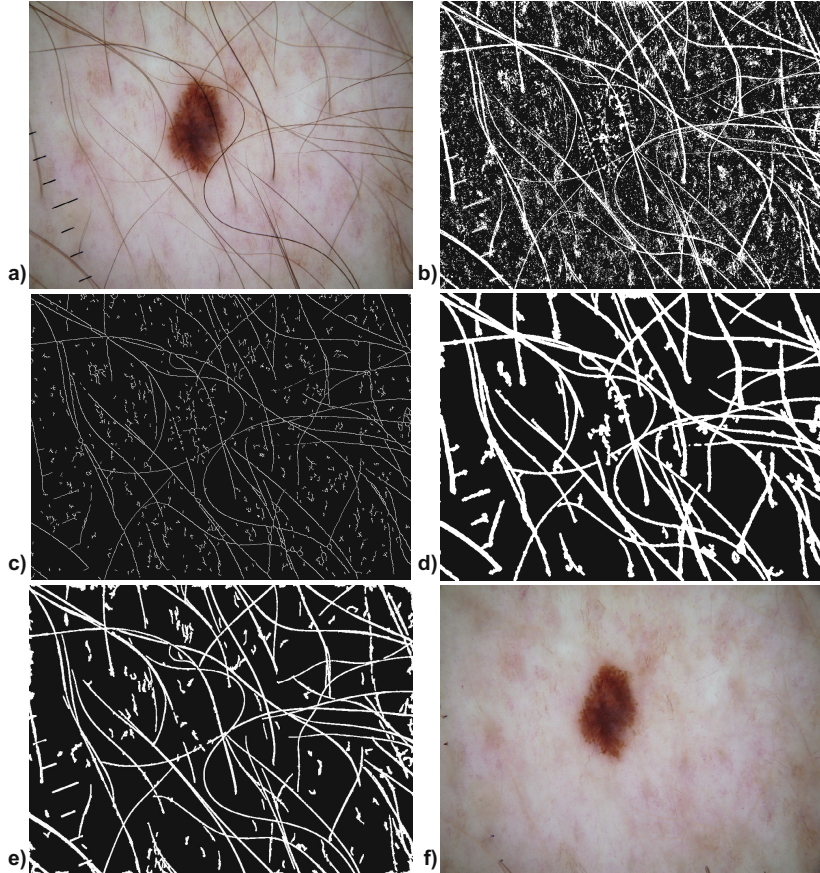


Fig. 1. a) Input image. b) Full hair mask M . c) Simplified mask skeleton S_M^τ . d) Filtered mask M^f . e) Mask created by [12]. f) Inpainted hair using M^f .

Morphological closing finds only hairs darker than skin. To find hairs lighter than skin, we replace closing by morphological opening. Having the dark-hair

and light-hair masks M^d and M^l , we can next either combine the two or select one mask to use further. We observed in virtually all our test images that dark and light hairs do not occur together. So, we use next the mask $M \in \{M^d, M^l\}$ that most likely contains hairs, *i.e.*, which maximizes the length of the longest skeleton-branch in $S_{\partial M}$. For example, for the image in Fig. 1 a, which has mainly dark hairs, our method will select to use the mask $M := M^d$ (Fig. 1 b).

3.3 False Positive Elimination

Since we search for gaps on *every* threshold-level, we find more gaps than traditional approaches, *e.g.* [18, 27, 14, 12]. Filtering out ‘false positives’ (gaps unlikely to be hairs), is thus necessary. We achieve this in four steps, outlined below.

Component Detection. First, we extract from M all 8-connected foreground components $C_i \subset M$. We skip components less than 1% of the size of image M , as these cannot possibly be elongated hairs. Remaining components are analyzed next to see if they are hairs or not.

Hair Skeletons. Hair fragments are long and thin. To measure such properties on our components C_i , we use their skeletons $S_{\partial C_i}$. Yet, components C_i may have jagged borders, due to input-image noise, shadows, or resolution limits (Fig. 1 b), so $S_{\partial C_i}$ have many short spurious branches. We discard these and keep each component ‘core’ by pruning each $S_{\partial C_i}$ as in [25]: From $S_{\partial \Omega}$, we produce a skeleton $S_{\partial \Omega}^\tau$ which keeps only points in $S_{\partial \Omega}$ caused by details of $\partial \Omega$ longer than τ . By making τ proportional to the component’s boundary length $\|\partial C_i\|$, we ensure that longer branches are pruned more than shorter ones. We also impose a minimum τ_{min} to discard tiny spurious fragments, and a maximum τ_{max} to preserve large branches. Hence, the pruning parameter τ for a component C_i is

$$\tau = \max(\tau_{min}, \min(\|\partial C_i\| \cdot \mu, \tau_{max})) \quad (6)$$

where $\mu \in [0, 1]$ is used as a scaling parameter. Figure 1 c shows the simplified skeleton $S_{\partial M}^\tau$ obtained from the mask M in Fig. 1 b.

Hair Detection. In DHR, finding if a component is thin and long is done by *e.g.* (a) fitting lines in a finite number of orientations and checking the length of the longest such line [18]; (b) using principal component analysis to find if the major-to-minor eigenvalue ratio exceeds a threshold [17]; and (c) computing an elongation metric comparing a component’s skeleton-length with its area [27]. Xie *et al.* argue that (a) and (b) are limited, as they favor mainly straight hairs and yield false-negatives for curled hairs [27]. They alleviate this by an elongation metric equal to the ratio of the area $\|C_i\|$ to the squared length of the ‘central axis’ of C_i ; but they give no details on how this central-axis (and its length) are computed. In particular, for crossing hairs, *i.e.*, when the skeleton of C_i has multiple similar-length branches, multiple interpretations of the notion of a ‘central axis’ are possible. We also found that (c) also yields many false-negatives, *i.e.*, marks as hair shapes which do not visually resemble a hair structure at all.

To address such issues, we propose a new metric to find if a thin-and-long shape is likely a hair. Let $J_i = \{\mathbf{x}_i \in S_{\partial C_i}^\tau\}$ be the set of junctions of $S_{\partial C_i}^\tau$, *i.e.*, pixels where at least three $S_{\partial C_i}^\tau$ branches meet. If the maximum distance

$d_{max} = \max_{\mathbf{x} \in J_i, \mathbf{y} \in J_i, \mathbf{x} \neq \mathbf{y}} \|\mathbf{x} - \mathbf{y}\|$ between any two junctions is small, then C_i is too irregular to be a hair. We also consider the average branch-length between junctions $d_{avg} = \|S_{\partial C_i}\| / \|J_i\|$, i.e., the number of skeleton-pixels divided by the junction count. If either $d_{max} < \delta_{max}$ or $d_{avg} < \delta_{avg}$, then C_i has too many branches to be a thin elongated hair (or a few crossing hairs), so we erase $S_{\partial C_i}$ from the skeleton image. Good values for δ_{max} and δ_{avg} are discussed in Sec. 6.

Mask Construction. We construct the final mask M^f that captures hairs by convolving the filtered skeleton-image (in which false-positives have been removed) with disks centered at each skeleton-pixel \mathbf{x} and of radius equal to $DT_{\partial M}(\mathbf{x})$. Figure 1d shows the mask M^f corresponding to the skeleton image in Fig. 1c. Comparing it with the hair-mask produced by [12] (Fig. 1e), we see that our mask succeeds in capturing the same amount of elongated hairs, but contains fewer small isolated line-fragments (thus, has fewer false-positives).

3.4 Hair Removal

We remove hairs by using classical inpainting [24] on the hair-mask M^f . To overcome penumbras (pixels just outside M^f are slightly darker due to hair shadows), which get smudged by inpainting into M^f , we first dilate M^f isotropically by a 3×3 square structuring element. This tells why hairs in M^f in Fig. 1d are slightly thicker than those in Fig. 1b. Figure 1f shows our final DHR result.

4 Implementation

The most expensive part of our method is computing M , which requires distance transforms and skeletons from up to 256 binary images (Sec. 3.2). As these images can be over 1024^2 pixels for modern dermoscopes, processing a single image must be done within milliseconds to yield an acceptable speed. For this, we use the GPU-based method for exact Euclidean distance transforms in [6]. A simple modification of this method allows us to compute dilations and erosions (by thresholding the distance transform with the radius of the disk structuring element) and simplified skeletons (by implementing the boundary-collapse in [25]). For implementation details, we refer to [28]. We also tested our method on multi-GPU machines by starting k MPI processes for k GPUs. Each process $p \in [0, k)$ does gap-detection on a subset of the threshold-set by launching CUDA threads to parallelize gap-detection at image block level [6]. The k separate masks $M_p, 1 \leq p \leq k$ are merged by process 0 into a single mask M , after which it continues with false-positive removal (Sec. 3.3). Connected component detection, done with union-find [21], and hair inpainting [24], are implemented in C++ on the CPU, as they are done on a single image.

5 Results and Comparison

Material. We have tested our method on over 300 skin images. These cover a wide range of skin lesions; hair thickness, color, length, density; and skin colors, acquired by several types of dermoscopes, by three research groups. Some images contain no hair; they let us see how well can we avoid false positives. This is important, as removing non-hair details may affect subsequent analyses [2, 12].



Fig. 2. Comparison of our method with DullRazor [17] and Huang *et al.* [12]. Insets show details.

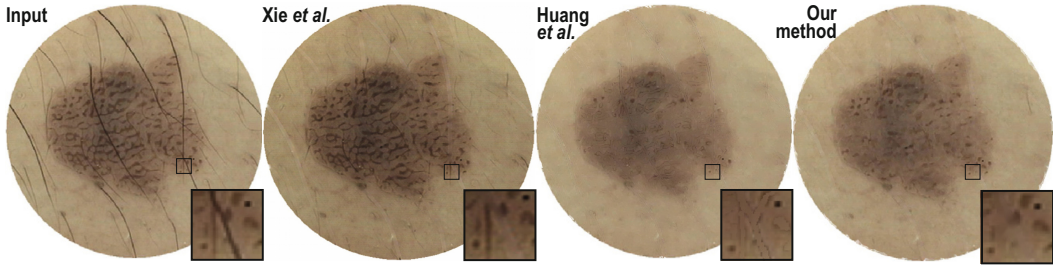


Fig. 3. Comparison between Xie *et al.* [27], Huang *et al.* [12], and our method

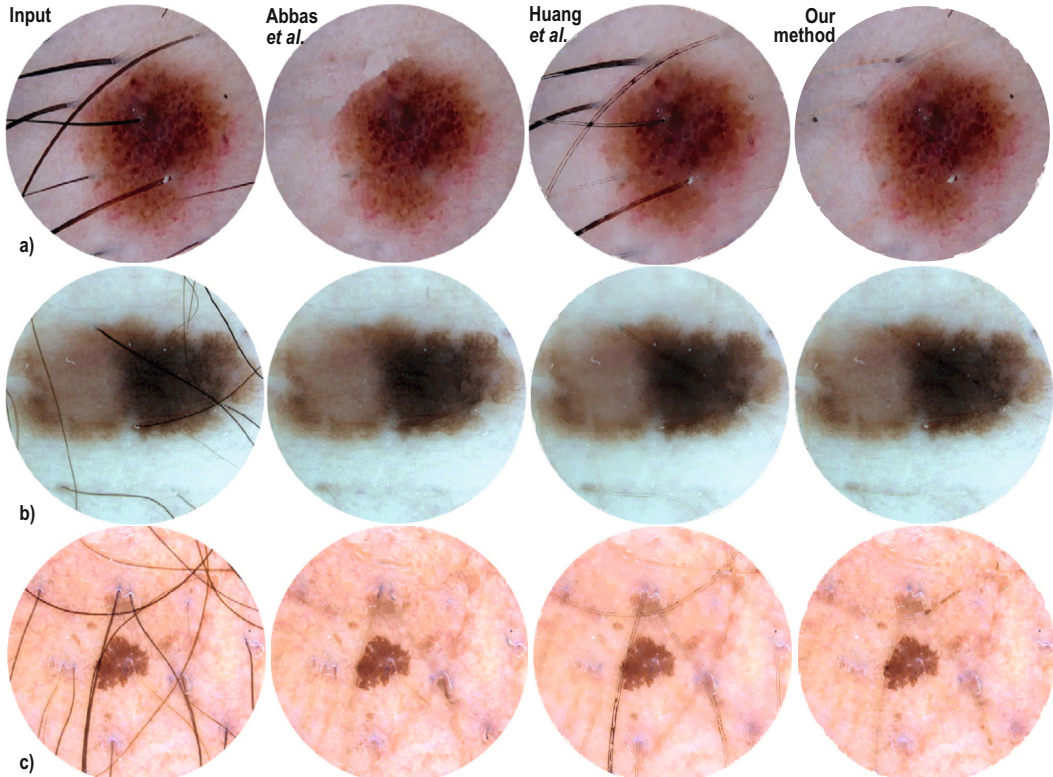


Fig. 4. Comparison between Abbas *et al.* [2], Huang *et al.* [12], and our method

Methods. We compare our results with five DHR methods: Where an implementation was available [18,12], we ran our full image-set through it. For the other methods [27,2,11], we processed images from the respective papers.

Results. Compared to DullRazor and Huang *et al.* [12] (Fig. 2), we see that DullRazor cannot remove low-contrast hairs (a,d); and both methods create ‘halos’ around removed hairs (c,f;e,f). Images (g,h) show two complex lesions, with hair of variable tints, opacity, thickness, and density. For (g), we create less halos around removed hairs than both DullRazor and Huang *et al.* For (h), our method removes considerably more hair than both methods. Figure 3 compares our results with Xie *et al.* [27] and Huang *et al.* We remove more hairs than Xie *et al.*, but also remove a small fraction of the skin. Huang *et al.* removes all hairs but also massively blurs out the skin. This is undesirable, since such patterns are key to lesion analysis. Figure 4 compares our method with Abbas *et al.* [2] and Huang *et al.* We show comparable results to Abbas *et al.* Huang *et al.* has issues with thick hairs (a) and also creates undesired hair halos (c). Compared

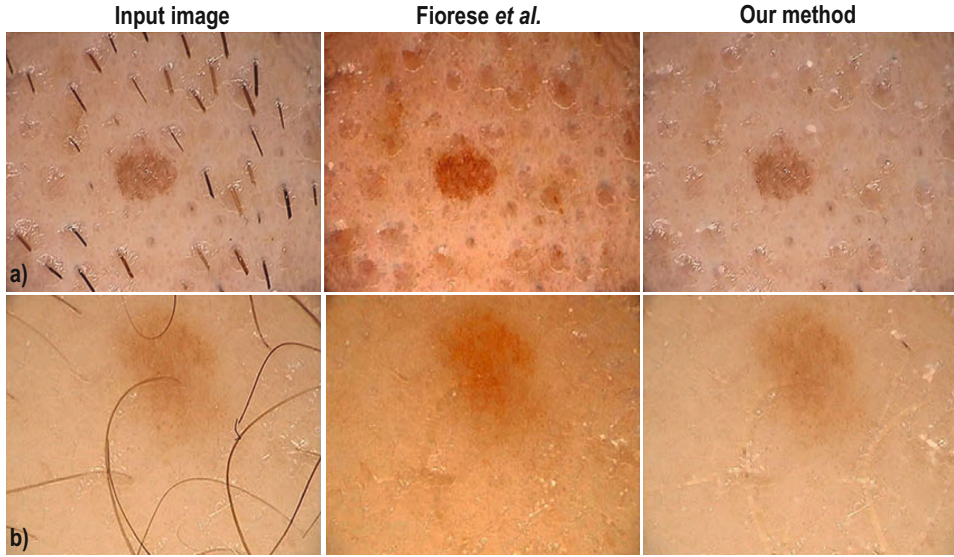


Fig. 5. Comparison between Fiorese *et al.* [11] and our method

to Fiorese *et al.* [11], we show a similar ability in removing both stubble and elongated hairs (Fig. 5). Strikingly, Fiorese *et al.* changes the hue of the input image, which is undesired. Our method correctly preserves the hue of the image.

Validation. We have shown the input images, and obtained DHR results, to two dermatologists having over 11 years of clinical experience. We asked whether the two images would lead them to different interpretations or diagnoses. In all cases, the answer was negative. While a more formal, quantitative, test would bring additional insight, this test tells that our DHR method does not change the images in *undesirable* ways. Separately, hair removal is obviously *desirable*, *e.g.* when using images in automated image-analysis procedures [2,12].

Other Applications. Our method can be used beyond DHR. Figure 6 shows an use-case for cone-beam computed tomography (CBCT) images. Positron emission tomography (PET) is a functional imaging modality used to deduce the spatial distribution of a radio-labelled substance injected into a subject. To put PET data in spatial context, high-resolution CBCT images can be acquired and co-registered with PET data. Two types of sensors are inserted into the subject (a mouse under physiological monitoring): soft plastic tubes (S) and hard metal wires (H). H sensors cause streak artifacts, making the CBCT reconstruction (onto which the PET data is overlaid) unusable. Hence, we want to automatically remove them. Doing this by using the CBCT volume is possible but quite expensive and complex. We remove such artifacts directly from the 2D X-ray images used to create the CBCT volume. Our DHR method is suitable for this, since the H implements appear as thin, elongated, and dark 2D shapes in such projections (see Figs. 6 a-c). Figures 6 e-g show the H implement-removal results. As visible, the H implements present in the input images have been successfully detected and removed. In contrast, the S implements, which have lower contrast and are thicker, are left largely untouched. Figure 6 d shows the 3D reconstruction done from the raw X-ray images (without our artifact removal). In the lower part, the image is massively affected by streak artifacts. Figure 6 h shows the reconstruction done from our DHR-processed images. As visible, most streak

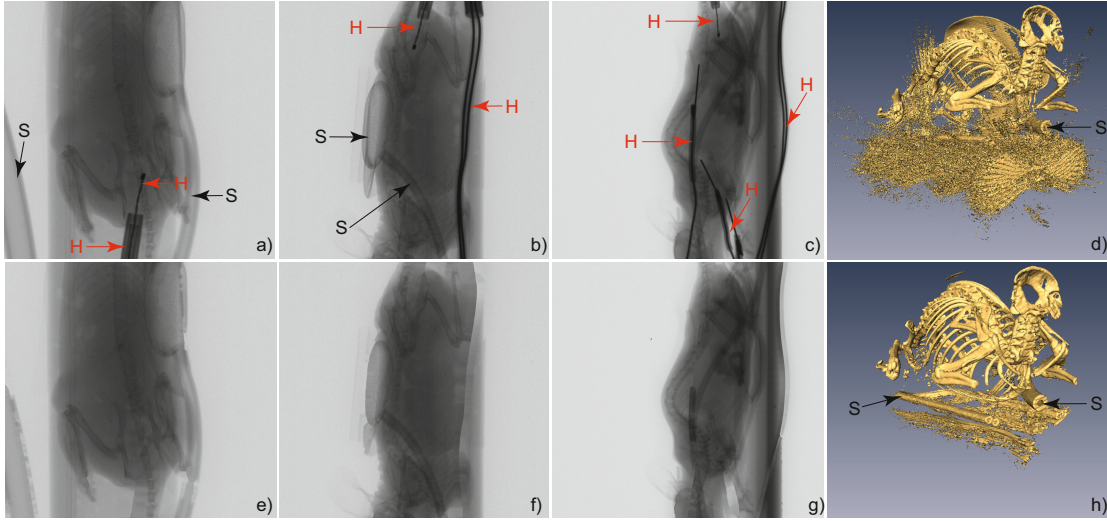


Fig. 6. Artifactual removal from CBCT images. (a-c) Input images, with soft (S) and hard metal-wire (H) artifacts. (e-g) Reconstructed images with removed wires. 3D volumetric reconstructions from original images (d) vs our images (h).

artifacts have been removed. In contrast, the thick soft (S) tubes have been preserved by our DHR method and the resulting reconstruction.

6 Discussion

Parameters. To obtain full automation, we ran our method on several tens of skin images (at resolution 1024^2), varying all its parameters, and selected those values which visually yielded the best results (most true-positive and least false-positive hairs). Next, we computed final parameters by averaging, and tested that these values give good results on our full image test-set. Table 2 presents the final parameter values, used to produce all images in this paper.

Table 2. Empirically established parameter values

	Description	Definition	Value
H	Structuring element radius	Section 3.2	5.0 pixels
λ	Gap detection parameter	Equation 4	0.2
μ	Skeleton simplification parameter	Equation 6	0.05
τ_{\min}	Minimum skeleton pruning	Equation 6	3.0 pixels
τ_{\max}	Maximum skeleton pruning	Equation 6	40.0 pixels
δ_{\max}	Hair detection parameter	Section 3.3	20.0 pixels
δ_{avg}	Hair detection parameter	Section 3.3	10.0 pixels

Robustness. We reliably remove hairs regardless of thickness, curvature, color, or underlying skin pattern. Very thin and low-contrast hairs or stubble may not get (fully) removed, as they are either not found in M^f or do not meet the elongation criteria (Sec. 3.3). Yet, such details do not influence further analysis tasks.

Speed. We compute an open-close, a close-open, a skeletonization, and a skeleton-to-shape reconstruction step for all 256 thresholds. For a 1024^2 pixel image, this takes 28 seconds on a MacBook Pro Core i7 with a GT 750M GPU,

and 18 seconds on a comparable desktop PC with a GTX 690. For the same image and desktop PC, DullRazor needs 4 seconds, Fiorese *et al.* 7 seconds, Abbas *et al.* 40 seconds, Xie *et al.* 150 seconds, and Huang *et al.* about 10 minutes.

Implementation. We use [6] to compute distance transforms on the GPU in linear time with the pixel count, and also multiscale skeletons and morphological openings and closings [28]. For inpainting, we use the simple method in [24]. C++ source code of our full method is available at [15].

Limitations. For very dense hairs of varying color on high-contrast skin (*e.g.* Fig. 2h), we cannot fully remove all hairs. Yet, this image type is extremely atypical. Also, other methods [18,12] remove significantly less hairs in such cases.

7 Conclusions

We have proposed a new approach for digital hair removal (DHR) by detecting gaps in all layers of an image threshold-set decomposition. We find false-positives by using medial descriptors to find thin and elongated shapes. We compared our method against five known DHR methods on a set of over 300 skin images – to our knowledge, is the broadest DHR method comparison published so far.

Machine learning techniques [3,16,9] could improve false-positive filtering. Further false-negative avoidance can be improved by extending our method to use additional input dimensions besides luminance, such as hue and texture.

Acknowledgement. This work was funded by the grants 202535/2011-8 (CNPq, Brazil) and PN-II RU-TE 2011-3-0249 (CNCS, Romania).

References

1. Abbas, Q., Fondon, I., Rashid, M.: Unsupervised skin lesions border detection via two-dimensional image analysis. *Comp. Meth. Prog. Biom.* 104, 1–15 (2011)
2. Abbas, Q., Celebi, M.E., García, I.F.: Hair removal methods: A comparative study for dermoscopy images. *Biomed Signal Proc. Control* 6(4), 395–404 (2011)
3. Altman, N.: An introduction to kernel and nearest-neighbor nonparametric regression. *The American Statistician* 46(3), 175–185 (1992)
4. Bertalmio, M., Sapiro, G., Caselles, V., Ballester, C.: Image inpainting. In: *Proc. ACM SIGGRAPH*, pp. 417–424 (2000)
5. Bornemann, F., März, T.: Fast image inpainting based on coherence transport. *J. Math. Imaging Vis.* 28, 259–278 (2007)
6. Cao, T., Tang, K., Mohamed, A., Tan, T.: Parallel banding algorithm to compute exact distance transform with the GPU. In: *Proc. ACM I3D*, pp. 83–90 (2010)
7. Christensen, J., Soerensen, M., Linghui, Z., Chen, S., Jensen, M.: Pre-diagnostic digital imaging prediction model to discriminate between malignant melanoma and benign pigmented skin lesion. *Skin Res. Technol.* 16 (2010)
8. Cokelaer, F., Talbot, H., Chanussot, J.: Efficient robust d -dimensional path operators. *IEEE J. Selected Topics in Signal Processing* 6(7), 830–839 (2012)
9. Cortes, C., Vapnik, V.: Support-vector networks. *Mach. Learn.* 20(3), 273–297 (1995)

10. Couprie, M., Bezerra, F.N., Bertrand, G.: Topological operators for grayscale image processing. *J. Electronic Imag.* 10(4), 1003–1015 (2001)
11. Fiorese, M., Peserico, E., Silletti, A.: VirtualShave: automated hair removal from digital dermatoscopic images. In: Proc. IEEE EMBS, pp. 5145–5148 (2011)
12. Huang, A., Kwan, S., Chang, W., Liu, M., Chi, M., Chen, G.: A robust hair segmentation and removal approach for clinical images of skin lesions. In: Proc. EMBS, pp. 3315–3318 (2013)
13. Iyatomi, H., Oka, H., Celebi, G., Hashimoto, M., Hagiwara, M., Tanaka, M., Ogawa, K.: An improved internet-based melanoma screening system with dermatologist-like tumor area extraction algorithm. *Comp. Med. Imag. Graph.* 32(7), 566–579 (2008)
14. Kiani, K., Sharafat, A.: E-shaver: An improved dullrazor for digitally removing dark and light-colored hairs in dermoscopic images. *Comput. Biol. Med.* 41(3), 139–145 (2011)
15. Koehoorn, J., Sobiecki, A., Boda, D., Diaconeasa, A., Jalba, A., Telea, A.: Digital hair removal source code (2014), <http://www.cs.rug.nl/svcg/Shapes/HairRemoval>
16. Kohonen, T.: Learning vector quantization. In: Self-Organizing Maps, pp. 203–217. Springer (1997)
17. Lee, H.Y., Lee, H.-K., Kim, T., Park, W.: Towards knowledge-based extraction of roads from 1m-resolution satellite images. In: Proc. SSIAI, pp. 171–178 (2000)
18. Lee, T., Ng, V., Gallagher, R., Coldman, A., McLean, D.: Dullrazor®: A software approach to hair removal from images. *Comput. Biol. Med.* 27(6), 533–543 (1997)
19. Nguyen, N., Lee, T., Atkins, M.: Segmentation of light and dark hair in dermoscopic images: a hybrid approach using a universal kernel. In: Proc. SPIE Med. Imaging, pp. 1–8 (2010)
20. Perona, P., Malik, J.: Scale-space and edge detection using anisotropic diffusion. *IEEE TPAMI* 12(7), 629–639 (1990)
21. Rahimi, A.: Fast connected components on images (2014), <http://alumni.media.mit.edu/~rahimi/connected>
22. Saugeon, P., Guillod, J., Thiran, J.: Towards a computer-aided diagnosis system for pigmented skin lesions. *Comput. Med. Imag. Grap.* 27, 65–78 (2003)
23. Sobiecki, A., Jalba, A., Boda, D., Diaconeasa, A., Telea, A.: Gap-sensitive segmentation and restoration of digital images. In: Proc. EG GVC, pp. 136–144 (2014)
24. Telea, A.: An image inpainting technique based on the fast marching method. *J. Graphics, GPU, & Game Tools* 9(1), 23–34 (2004)
25. Telea, A., van Wijk, J.J.: An augmented fast marching method for computing skeletons and centerlines. In: Proc. VisSym, pp. 251–259 (2002)
26. Wighton, P., Lee, T., Atkins, M.: Dermascopic hair disocclusion using inpainting. In: Proc. SPIE Med. Imaging, pp. 144–151 (2008)
27. Xie, F., Qin, S., Jiang, Z., Meng, R.: PDE-based unsupervised repair of hair-occluded information in dermoscopy images of melanoma. *Comp. Med. Imag. Graph.* 33(4), 275–282 (2009)
28. Zwan, M.v.d., Meiburg, Y., Telea, A.: A dense medial descriptor for image analysis. In: Proc. VISAPP, pp. 285–293 (2013)